Chapter 3
Cold Atmospheric Plasma Sources for Cancer Applications and Their Diagnostics

Eun Ha Choi

Contents

Abstract In general, the plasma used for the cancer therapy could be generated at the atmospheric pressure state under ambient air environment by injecting other kinds of gases such as He, Ar, nitrogen, water molecules, and their mixture for appropriate applications. This plasma should have following safety characteristics for cancer treatment such as nonthermal or cold temperature (less than 40 °C) characteristics, low electrical leakage currents to skin (less than 100 uA) for no electrical shock, and as low as amount of ozone generation (less than 0.05 ppm) for breathing safety. This kind of plasma is called as "nonthermal atmospheric pressure plasma (NAPP)," or "nonthermal biocompatible plasma (NBP)," or "cold atmospheric pressure plasma (CAP)." In addition, this plasma should be easy-handled for clinical test.

This chapter describes specific plasma devices for cancer application and their diagnostics.

E. H. Choi (✉)
Plasma Bioscience Research Center (PBRC), Kwangwoon University, Seoul, South Korea
e-mail: ehchoi@kw.ac.kr

© Springer Nature Switzerland AG 2020

M. Keidar (ed.), *Plasma Cancer Therapy*, Springer Series on Atomic, Optical, and Plasma Physics 115, https://doi.org/10.1007/978-3-030-49966-2_3

3.1 Plasma Sources

3.1.1 Soft Plasma Jet

Plasma jets (see Chap. 2 for detailed description) are one of the simplest atmospheric plasma sources that could be created in the laboratory. Plasma jet is generated by using noble gas and has a benefit of producing long plasma plumes [1–4]. The soft plasma jet as shown in Fig. 3.1, it is consisting of an inner syringe needle acing as a high voltage (HV) electrode and gas inlet which covered and connected with quartz tube. Quartz tube serves as a guide for the plasma jet flow and is designed to induce dielectric discharge through the sheet current along the concave part at the end of the quartz tube between the grounded electrode and the needle. The distance between the needle tip and the grounded electrode is 2–3 mm and the plasma jet plume produced along 5 mm from nozzle. Soft plasma jet discharge operates using the HV inverter. Porous alumina with a diameter of 10–12 mm and a length of 17–20 mm could be machined and placed in tight contact between the two electrodes of the inner and outer electrodes according to the applications. The porous alumina if used in this work is approximately 30 vol % porosity with an average pore diameter of 80–100 um. Gas is injected into the injection needle and then ejected through the 1–2 mm hole in the outer electrode. Air or any other gases could be used as the feeding gas; the flow rate is controlled by an analog or mass flow controller. Once gas is introduced through the inner electrode and high-voltage ac power from inverter is applied, a discharge is fired into the porous alumina between the electrodes and a long plasma jet reaching lengths of up to 10 mm is ejected into the open air. Cells or biological targets were treated with jet plasma for appropriate exposure times such s 30 s, 60 s, 120 s, and 240 s under an electrical discharge power of less than about 2 W (Vpeak: 1–2 kV and Ip: 1–2 mA) from a duty-cycle controlled inverter voltage. The driving frequency is 20–50 kHz and flow rate of air gas is kept to 1–2 liter per minute (lpm). The working temperature of the plasma source is in the range of 26-36 °C at the time of treatment.

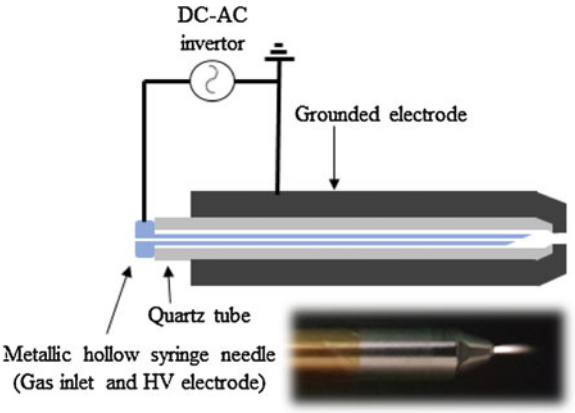

Fig. 3.1 Schematic of soft plasma jet

3.1.2 μ-DBD (Micro-Dielectric Barrier Discharge) Plasma

Since the first study by Ernst Werner von Siemens in 1857, there have been various forms of dielectric barrier discharge (DBD) plasma source development. Figure 3.2 shows a nonthermal atmospheric pressure surface micro-dielectric barrier discharged (u-DBD) (S u-DBD) plasma for the coplanar electrodes [5] (a) and facing DBD (F u-DBD) electrodes [6] (b). Biological skins could be treated by these kinds of DBD plasma for 30 s—few minutes under electrical discharge power of about less than 3 W (1–2.2 kV, 1–2 mA, and phase angle 0.7 radian) with duty-cycle controlled high-voltage ac inverter or commercial high voltage used for neon light. The driving frequency of sinusoidal high voltage could be controlled to be 60 Hz to 100 kHz as well as its duty cycles 1–50%. The electrical discharge is sustained by alternating high voltage applied to the two electrodes covered by dielectric materials whose thickness is about 100 um. The dielectric materials could be chosen appropriately among glass, quartz, ceramics, and polymers for purposes. The distance between the electrodes can be varied from a distance of less than 0.1 mm to several centimeters. As shown in Fig. 3.2, typical u-DBD discharge occurs between two electrodes separated by an insulating dielectric barrier in surface u-DBD (S u-DBD) (a) and facing u-DBD (F u-DBD) (b). At S u-DBD micro-discharges occur on the coplanar dielectric surface, and plasma generation is more uniform than F u-DBD. The Fig. 3.3 shows typical fabrication processes for S u-DBD electrodes based on the semiconductor processing. The two parallel electrodes are made of Ag paste film patterned by screen printing method with drying and furnace treatment under 600 °C on the glass or ceramic substrate. Finally, aluminum oxide Al_2O_3 film has been deposited to be 1 um in thickness on the SiO_2 dielectric barrier by either e-beam evaporation or sputtering method for lowering the breakdown voltage in plasma generation.

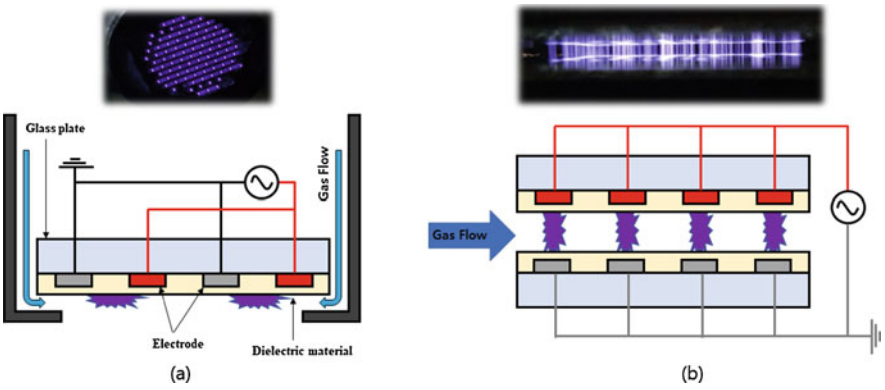

Fig. 3.2 Schematic of u-DBD electrode structure (**a**) Surface u-DBD(S u-DBD), (**b**) Facing u-DBD(F u-DBD)

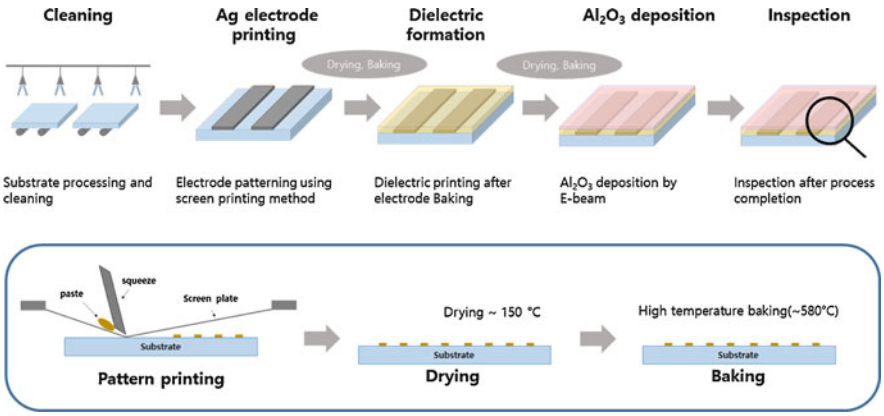

Fig. 3.3 Surface u-DBD electrode manufacturing process

The separation of these coplanar two electrodes were kept to by 100–200 um, whose thickness are about 3–5 um, after that they are tightly covered with insulating SiO_2 thick film by screen printing method. The thickness of substrate is about 1.8 mm. The diameter of u-DBD surface plasma is 30–100 mm, which is designed for 20–100 mm petri-dishes. The discharge power is about less than 3 W whose peak voltage is about Vp ~ 1–2 kV and currents are less than 5 mA. Working temperature of plasma source is in the range of 24–32 °C at the time of treatment.

3.2 Electrical and Optical Characteristics of Plasma Sources for Cancer Applications

3.2.1 Electrical Characteristics

An oscilloscope (DSO-X-3104T, Keysight) was used to measure the voltage and current of the discharge between the electrodes. As shown in Fig. 3.4, the voltage was measured between the HV electrode (syringe needle) and the grounded electrode using an HV probe (P6015A, Tektronix). The current was measured using a current probe (P6021, Tektronix).

Figure 3.5 shows an output voltage (a) of the HV inverter for soft plasma jet with voltage duty ratio controlled for minimization of heat damage and ozone production during plasma discharge. The discharge of the soft plasma jet has been generated by 2 kV and 50 kHz sinusoidal wave (b) under the nitrogen or any other gas flow rate of 1.5 lpm. The discharge on-time duration is fixed to be 25 ms, and the duty ratio could be adjusted by 9–14% by controlling the off-time duration in the driving voltage. In Fig. 3.6a, output voltage of the HV inverter for surface u-DBD has a voltage duty ratio to minimize the heat damage and ozone caused by plasma discharge like Fig.

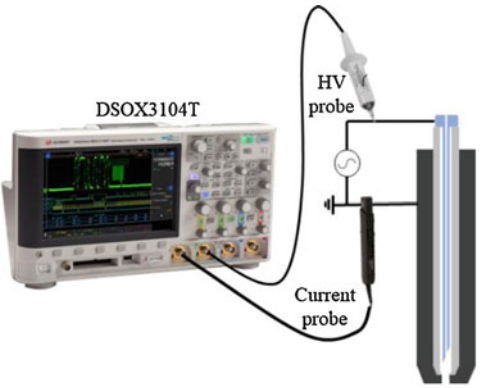

Fig. 3.4 Electrical measurement of plasma source

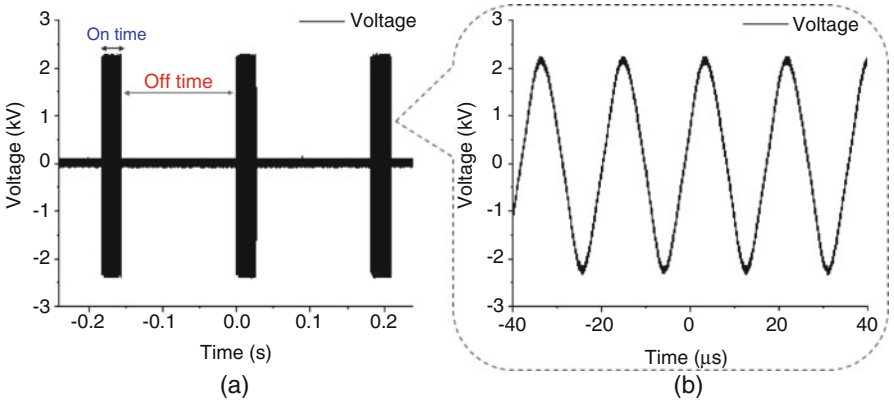

Fig. 3.5 Voltage waveform from high voltage invertor for soft plasma jet (**a**) on-off time of high voltage invertor, (**b**) 2 kV, 50 kHz sinusoidal wave

3.5a. The discharge of the surface u-DBD plasma has been generated by 1.5 lpm of nitrogen gas and the sinusoidal driving voltage of 2 kV, 30 kHz as in Fig. 3.6b. The discharge on-time is fixed at 25 ms, and the duty ratio in driving voltage could be adjusted to be 9–14% by controlling the discharge off-time duration. The electrical energy per second could be obtained from the following equation with signal period T.

$$\text{Electrical energy per second} = \left(\frac{\text{On time}}{\text{On time} + \text{Off time}}\right) * \frac{1}{T}\int_0^T (V(t) * I(t))\, dt \tag{3.1}$$

The voltage and current waveforms used for the soft jet and surface u-DBD plasma are shown in the left-hand side and right-hand side of Fig. 3.7a, respectively. Positive discharge for soft jet and surface u-DBD plasma occur at voltage enhancement of (820 V, 880 V) with a discharge current of (40 mA, 10 mA), while a negative

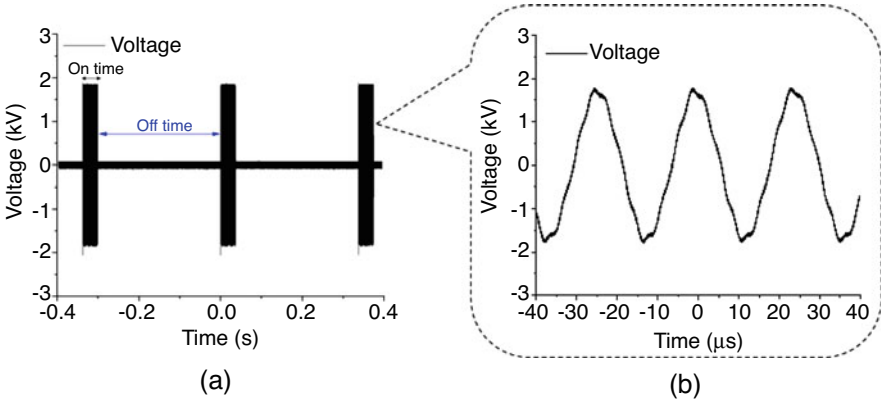

Fig. 3.6 Voltage waveform from HV invertor for S u-DBD (**a**) on-off time of HV invertor, and (**b**) 2 kV, 30 kHz sinusoidal wave in on-time

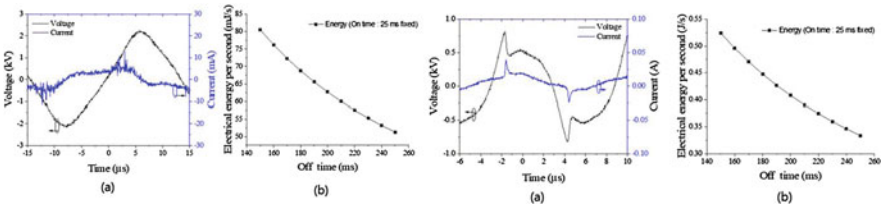

Fig. 3.7 Electrical characteristics of soft plasma jet (left-hand side) and S u-DBD plasma (right-hand side), (**a**) voltage (black line) and current (blue line) curve in discharge, (**b**) Electrical energy per second with duty ratio, respectively

discharge occurs at voltage enhancement of (−820 V, −800 V) with a discharge current of (−25 mA, −10 mA), respectively, in which the voltage frequency for the soft jet has been increased to 85 kHz from 50 kHz, while it has not changed for surface u-DBD plasma. The electrical energy has been performed for several off-time durations. Electrical energy per unit time also has been measured to be 350–520 mJ/s and 50–80 mJ/s for the soft jet and surface u-DBD plasma, respectively, where they are linearly decreased in accordance with off-time durations as shown in Fig. 3.7b.

3.2.2 Physical Characterization Measurement Methods

Ozone could be measured in accordance with the measurement distance from the nozzle of the soft plasma jet using commercial device (200 series, aeroqual), as shown in Fig. 3.8a. The gas temperature could also be measured by a fiber optic thermometer (FOT Lab kit, Luxtron), and this optical fiber for the measurement

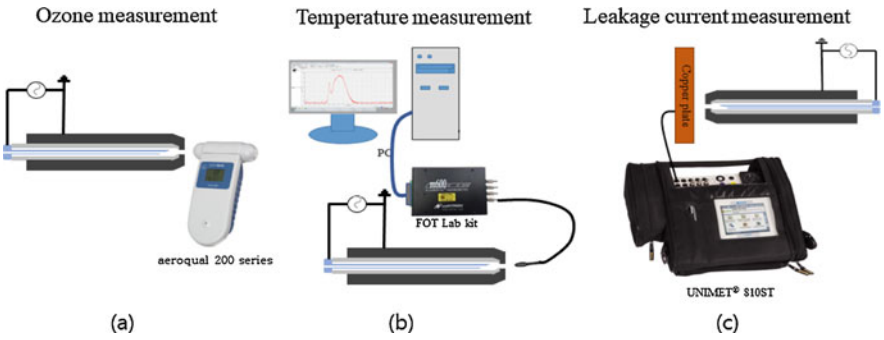

Fig. 3.8 Medical requirement limitation measurement; (**a**) ozone measurement, (**b**) axial temperature measurement, (**c**) leakage current measurement

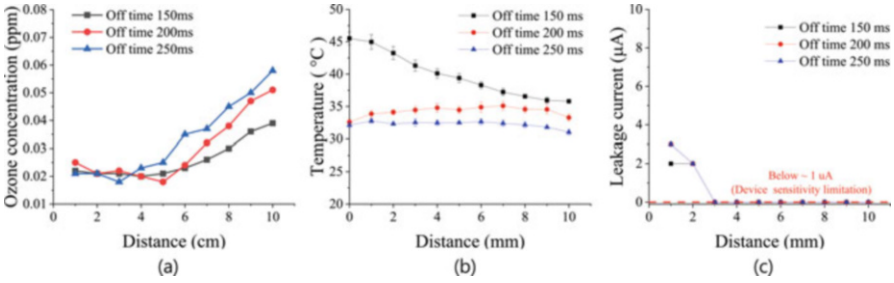

Fig. 3.9 Ozone concentration (**a**), temperature (**b**), and leakage current (**c**) measurement versus distance under several off-time durations in discharge for soft plasma jet

could be moved along the distance away from the discharge, as shown in Fig. 3.8b. Measurement results for temperatures have been time-averaged over a minute with resolution time of 1 s. Leakage current for the soft jet could also be measured by a copper plate target ($40 \times 40 \times 5$ mm^3) connected to a test device (UNIMET® 800ST, BENDER), as shown in Fig. 3.8c, according to the axial distance [7]. Optical emission spectroscopy (OES) has also been measured using a CCD spectrometer (HR4000, Ocean optics) and this OES has been performed with a distance of 1 cm away from either the plasma nozzle in soft plasma jet or u-DBD discharged plasma surface.

In Fig. 3.9a, ozone production from the soft plasma jet has been measured as increasing with distance, and it has been a little bit increased in accordance with increasing in off-time duration. The temperature has been found to be decreased by increasing either position of measurement distance or cooling off-time duration, as shown in Fig. 3.9b. As shown in Fig. 3.9c, leakage current has been measured and detectable up to only 2 mm from the soft jet nozzle, and no more leakage current has been measured beyond 3 mm from the nozzle since the lower measurement limit of the instrument is 1 uA.

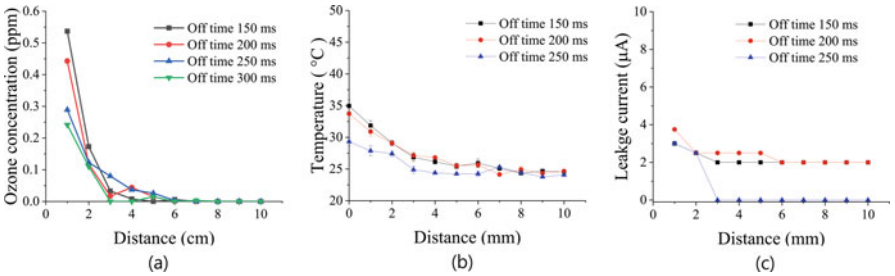

Fig. 3.10 Ozone, temperature, and leakage current measurement versus distance from surface of discharged u-DBD plasma for several off-time durations, (**a**) ozone concentration, (**b**) temperature, and (**c**) leakage current for surface u-DBD plasma

Figure 3.10 shows ozone concentration (a) versus distance from the discharged surface from S u-DBD plasma. It has been measured to maximum 0.55 ppm at 1 mm distance and it decreases with increase in measurement distance. The ozone concentration has also been decreased by increasing the off-time duration. The temperature has been measured to be below 35 °C in S u-DBD, and it is also decreased by increasing the cooling off-time duration as shown in Fig. 3.10b. The leakage current has been decreased up to 3 mm, and saturated beyond 3 mm for off-time duration of 150–200 ms. For off-time duration of 250 ms the leakage current has been measured to be less than 1 uA, which is under the low limitation detectable value of device, as shown in Fig. 3.10c.

3.2.3 Electron Temperature Measurement

The collisional radiative model is based on the relative intensity of the nitrogen optical emission line and can be used to calculate the electron temperature of the plasma jet. The diagnosis of electron temperature could be performed based on the collisional radiative model (CRM) using the rate balancing equation between N_2 SPS (N_2 second positive system, $C^3\Pi_u \rightarrow B^3\Pi_g$) and N_2 FPS (N_2 first positive system, $B^3\Pi_g \rightarrow A^3\Sigma_u{}^+$) [8–11]. The rate equilibrium equation in the nitrogen molecule's transition model can be expressed through several reactions. First, the excitation reaction to the base states $X^1\Sigma_u{}^+$, $B^3\Pi_g$, and $C^3\Pi_u$ by electron excitation is the most important process, and the attenuation due to the collision, the wall deactivation reaction by the interaction with the surface, and the natural emission due to the transition to the lower energy level. The equilibrium equations for CRM are as follows [8].

$$n_e \sum_{\nu} n_{X,\nu} Q_{e-N_2}^{X,\nu \to A} + n_B \sum_{\nu} n_{X,\nu} Q_{N_2(B)-N_2(X)}^{B \to A} + A_B n_B \tag{3.2}$$

$$= n_A \sum_{5 \le \nu \le 14} n_{X,\nu} Q_{N_2(A)-N_2(X)}^{A \to B} + 2{n_A}^2 \left(Q_{N_2(A)-N_2(A)}^{A,\ A \to B} + Q_{N_2(A)-N_2(A)}^{A,A \to C} \right) + K_{\text{wall}}^{A} n_A$$

$$n_e \sum_{\nu} n_{X,\nu} Q_{e-N_2}^{X,\nu \to B} + n_A \sum_{\nu} n_{X,\nu} Q_{N_2(A)-N_2(X)}^{A \to B} + {n_A}^2 Q_{N_2(A)-N_2(A)}^{A,\ A \to B} + \sum_{\nu''} A_{C,\nu''} n_{C,\nu''} \tag{3.3}$$

$$= n_B \sum_{\nu} n_{X,\nu} Q_{N_2(B) \to N_2(X)}^{X,\nu \to C,\nu''} + A_B n_B$$

$$n_e \sum_{\nu} n_{X,\nu} Q_{e-N_2}^{X,\nu \to V,\nu''} + {n_A}^2 Q_{N_2(A)-N_2(A)}^{A,\ A \to C,\nu''} = A_{C,\nu''} n_{C,\nu''} \tag{3.4}$$

In the equilibrium equation above, n_e is the electron density, and n_x, n_A, n_B, and n_C denote excited density of $X^1\Sigma_u{}^+$, $A^3\ \Sigma_u{}^+$, $B^3\Pi_g$, $C^3\Pi_u$ energy levels, respectively. A is Einstein coefficient for transition, ν is the vibrational quantum number, and K_{wall} is the rate coefficient for wall deactivation [9, 10]. Q is a reaction constant for electron excitation in gaseous state [9–11] under assumptions of Maxwell electron energy distribution. The densities n_x, n_A, n_B, and n_C on each excited level could be obtained by using the above Eqs. (3.2), (3.3), and (3.4). The ratio of the emission line is obtained by using the emission intensities of N_2 SPS and N_2 FPS. The formula for the ratio R_1 of emission lines is as follows.

$$R_1 = \frac{A_C n_C\,(T_e)}{A_B n_B\,(T_e)} = \frac{I_C}{I_B} \tag{3.5}$$

Electron temperature could be calculated from cross point of theoretical value from Eq. (3.5) with electron temperature and experimental determined value of $R_1 = 28.88$, which is given by Eq. (3.5).

Figure 3.11 shows the OES of the soft plasma jet, where N_2 SPS (297–400 nm) and N_2 FPS (550–800 nm) are observed. The electron temperature has been measured to be 1.76 eV based on CRM model.

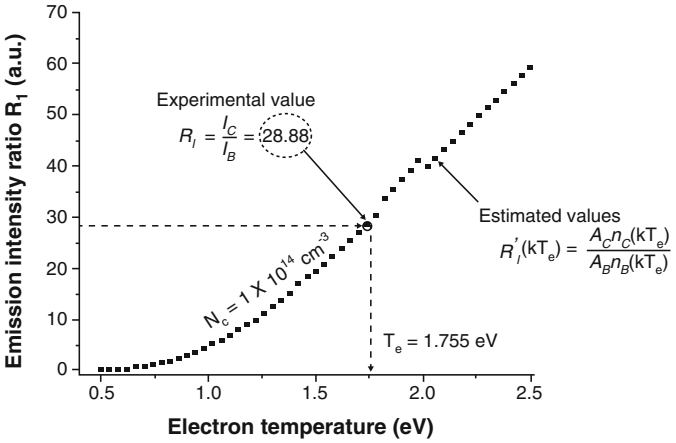

Fig. 3.11 Cross point of experimental value R_1 and estimated values [9–11]

3.2.4 Plasma Electron Density

Electron density in plasma is an important parameter to understand the formation of various reactive oxygen and nitrogen species in plasma jets. The electron density could be estimated using convective wave packet model from the jet current measurements [12]. Electron flux Γ_e might be a little greater than ion flux Γ_i due to electron has bigger diffusion coefficient, D_e than that of ion diffusion coefficient, D_i as well as $\upsilon_e \gg \upsilon_i$ where υ_e is electron mobility and υ_i is ion mobility, respectively. Therefore, the current density of plasma region could be expressed by

$$J = e\left(\Gamma_i - \Gamma_e\right) = e\left[\left(D_e - D_i\right)\nabla n + n\left(\upsilon_e + \upsilon_i\right)E\right] \approx e\left[D_e \nabla n + n\upsilon_e\, E_{\text{total}}\right] \approx en_e v_e \tag{3.6}$$

where e is the electron charge, A is the cross-sectional area of the plasma, v_e is the electron speed, and n_e represents the electron density. From this background reason, the downstream current density is not zero, i.e., $J \neq 0$, whenever we measured it in this experiment. It could be interpreted that the current density might be expressed almost by electron flux only. In addition, the ambipolar electric field E_{polar} causes ambipolar diffusion for $\Gamma_e \approx \Gamma_i$, the electron speed v_e should be close to ambipolar diffusion velocity, v_n. Therefore, current density in downstream region could be expressed by [12–16]

$$J \approx en_e v_e \approx en_e v_n \tag{3.7}$$

which is dominant electron flux under conditions of $\Gamma_e \approx \Gamma_i$. Therefore, the electron density could be estimated by using Eq. (3.3). The ambipolar diffusion

velocity has been estimated to be 3.30×10^2 m/s [12]. The peak value of downstream electron current has been measured to be about Ipeak $\approx$ 12 mA with plasma bullet radius of $r_b = 2.67 \times 10^{-4}$ m in this experiment. The electron density has been estimated to be 3×10^{15} cm^{-3} from Eq. (3.7) based on ambipolar diffusion model [12].

3.2.5 *Rotational and Vibrational Temperature Measurement Method*

Determination of the molecular gas temperature is of fundamental importance for understanding the characteristics of the plasma jet, as it plays the role of plasma thermometer. In nitrogen containing plasmas, the rotational distribution of nitrogen quickly achieves thermodynamic equilibrium within the gas, due to the faster exchange of rotational energy with heavy particles than with electrons. The Boltzmann distribution of rotational levels can be used to estimate the rotational temperature in such plasmas [17]. Optical emission spectroscopy has been extensively used to estimate the rotational temperature in nonthermal plasma jets [13, 17, 18]. Bruggeman et al. showed that more accurate value of gas temperature could be obtained using the N_2 (C–B), so called the second positive system (SPS) emission band [19] rather than the first positive system (FPS), where their transition energy diagram and real emission spectra are shown in Fig. 3.12a and b, respectively. Figure 3.12b shows the OES of the soft plasma jet, where N_2 SPS (297–400 nm) and N_2 FPS (550–800 nm) are observed. The OES spectrum from the surface u-DDB plasma is similar to that of soft jet as in Fig. 3.12b, where NO-γ band (213–258 nm), N_2 SPS, and N_2 FPS could also be observed [20]. The electron temperature for the soft jet and the surface u-DDB plasma have been measured to be 1.76 eV and be 0.6 eV based on CRM model and electron density for them have been estimated to be 3×10^{15} cm^{-3} and 5×10^{14} cm^{-3} from ambipolar diffusion model, respectively. Especially, optical emission spectroscopy (OES) at interfacial region of the biosolutions is extremely useful for bioplasma jet bombarding onto the surface since the informations for induced ROS and their spatial distribution characteristics could be obtained from these data.

In this work, we have selected rotational levels of the SPS belonging to the 0–0 vibrational band of N_2 ($C^3\,\Pi_u$) ($v = 0$) $- B^3\Pi g$ ($v = 0$), as indicated by magnified spectrum around 337 nm, in Fig. 3.12c. The intensity of a particular rotational band in this SPS is given by: [17]

$$I_{\text{em}} = C\left(J' + J'' + 1\right)\exp\left(-\frac{B'_v hc}{k_B T_{\text{rot}}} J'\left(J' + 1\right)\right) \tag{3.8}$$

where, C is a constant for a single band, $J^{'}$ and $J^{''}$ are the rotational quantum numbers for the transitions ($\upsilon^{'} = 0, J'$) ➔ ($\upsilon' = 0, J^{''}$), $B^{'}{}_{\upsilon}$ is the rotational term, h

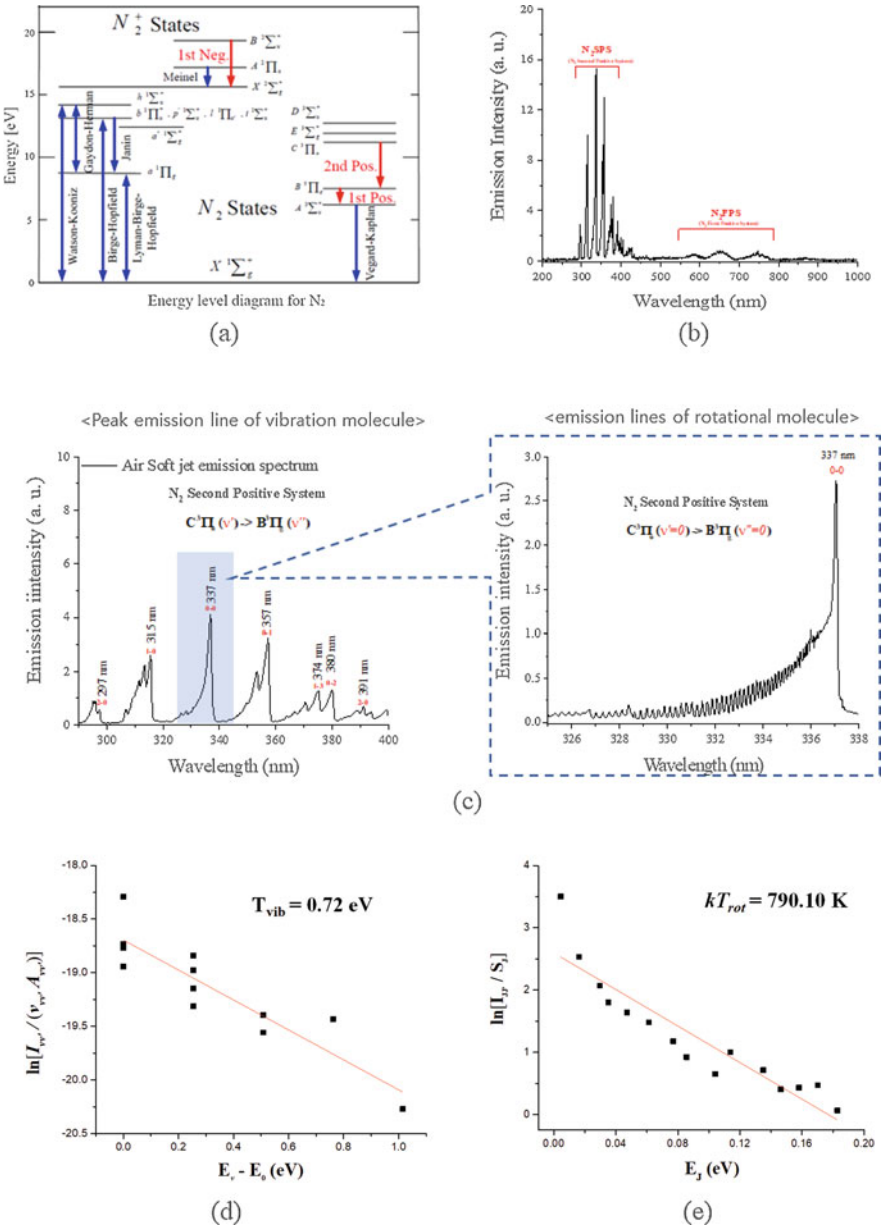

Fig. 3.12 Transition energy diagram N_2 (297–400 nm), so called the second positive system (SPS), emission band and N_2 (550–800 nm), so called the first positive system (FPS) (**a**) and their real emission spectra (**b**), respectively. Vibrational spectra of the N_2 SPS and magnified rotational spectrum belonging to the 0–0 vibrational band around 337 nm of N_2 (C^3 Πu) (v = 0) − B^3Πg ($v = 0$), as indicated by dotted box (**c**). Rotational temperature of 790.10 K (**d**), and vibrational temperature of 0.72 eV (**e**) for 1 mm irradiation position of plasma jet above the water surface, respectively

is Planck's constant, c is the velocity of light, k_B is the Boltzmann constant, and T_{rot} is the rotational temperature. For the estimation of rotational temperature, Eq. (3.8) can be rearranged as:

$$\ln\left(-\frac{I_{\text{em}}}{J'+J''+1}\right) = \ln C - \frac{B'_{\upsilon} hc}{k_B T_{\text{rot}}} J'\left(J'+1\right)\Big) \tag{3.9}$$

If the left-hand side is plotted against $J'(J'+1)$, the slope of the resulting linear distribution will be equal to $B_{\upsilon}{}^{'}$ hc/($k_B T_{\text{rot}}$), yielding the rotational temperature of the molecule. Figure 3.12d shows the rotational temperature calculated very close to the water surface for the 1 mm irradiation position of the plasma jet. From repeated experiments, the value is estimated to be 790.10 ± 2.43 °K. In this work, we have also selected vibrational levels of the SPS belonging to the υ–υ' vibrational band of N_2 ($C^3\,\Pi_u$) (υ) − $B^3\Pi g$ (υ'), as indicated by Fig. 3.12c. The intensity of a particular vibrational band in this SPS is given by [17],

$$\ln\left(\frac{I_{\upsilon\upsilon'}}{\nu_{\upsilon\upsilon'} A_{\upsilon\upsilon'}}\right) = \text{Constant} - \frac{E_{\upsilon} - E_0}{kT_{\text{vib}}} \tag{3.10}$$

where E_{υ} is given by

$$E_{\upsilon}(eV) = 1.2398 \times 10^{-4}\left(\frac{1}{2}+\upsilon\right)\left[\omega_e(\text{cm})^{-1}\right] \tag{3.11}$$

If the left-hand side of Eq. (3.10) is plotted against $E_{\upsilon} - E_o$, the slope of the resulting linear distribution will be equal $to 1/(kT_{\text{vib}})$, yielding the vibrational temperature of the gas molecules. Figure 3.12e shows the vibrational temperature calculated very close to the water surface for the 1 mm irradiation position of the plasma jet. From repeated experiments, the value is estimated to be 0.72 eV.

3.2.6 Radical Species OH Measurement Methods

For measurement of hydroxyl radical OH density, the nonthermal plasma jet has been in contact with the biosolution surface and its optical emission signal has been observed by charge-coupled device (CCD) spectrometer connected by the double slit and optical fiber with collimator lens [21]. Figure 3.13 shows the optical emission spectrum for Ar plasma jet measured by CCD spectrometer with optical fiber at the 2 mm above the deionized (DI) biosolution surface (a), and 2 mm below the DI biosolution surface (b). From the result of spectrum of Fig. 3.13a, the Ar emission lines between 700 nm and 900 nm are shown to be dominantly appeared and it is found that the 309 nm emitted from the hydroxyl OH radical [22–24] species, 224 nm from the nitric oxide NO [25], the emission lines 245 nm from the reactive species of superoxide anion $O_2{}^{*-}$ [26], and the emission lines from

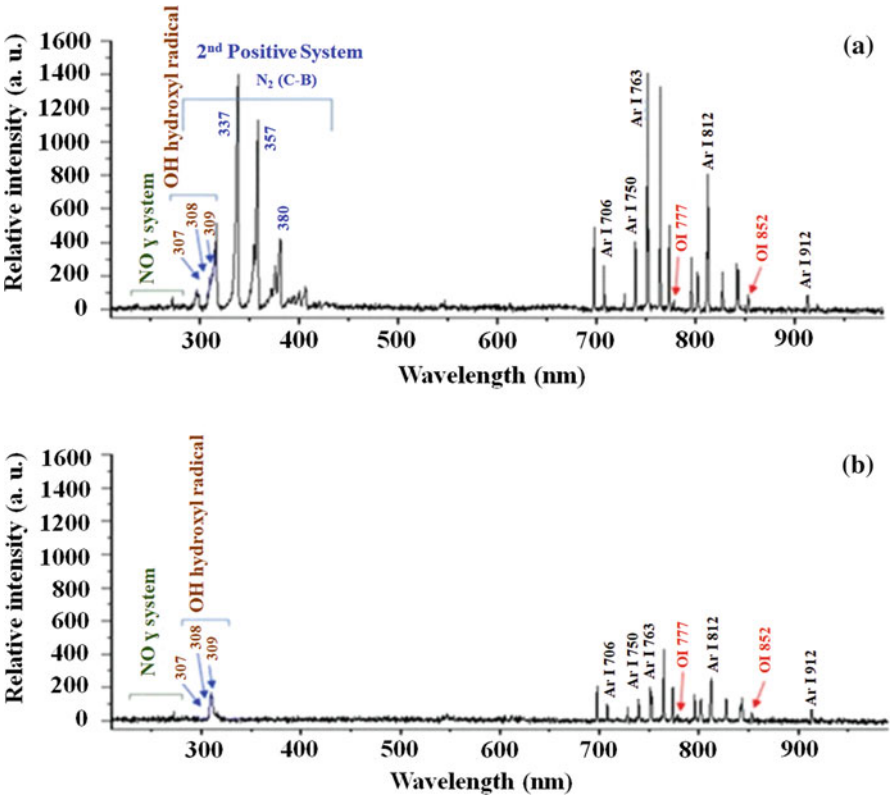

Fig. 3.13 Optical emission spectrum measured by CCD spectrometer with optical fiber at 2 mm above DI water (**a**), and 2 mm below the deionized (DI) surface (**b**) [21]

N_2 second positive system ($C^3\Pi u–B^3\Pi g$) ranged from 320 nm to 380 nm strongly appeared just above the biosolution surface. While as seen in Fig. 3.13b, as moved 2 mm downward into the DI biosolution surface, the emission lines of 224–280 nm from the nitric oxide NO [25], the 245 nm from the reactive species of superoxide anion O_2^{*-} [26], and N_2 second positive system ($C^3\Pi u–B^3\Pi g$) emission lines ranged from 320 nm to 380 nm are shown to be drastically disappeared. However, it is found that the 309 nm emitted from the hydroxyl OH radical species is getting weaker in the biosolution than that above the surface. It is also noted from the Figs. 3.13a and b that the both lines of 777 nm and 852 nm inside the DI biosolution, which are emitted from the O_2 first positive system, including the emission lines of Ar I and N_2 first positive system (B–A) are getting weaker than those above the solution.

Also we have measured the reactive oxygen species, especially, for the hydroxyl OH radicals by the optical emission spectroscopy as well as its absolute density inside or just interfacial region of the biosolutions by the ultraviolet (UV) absorption

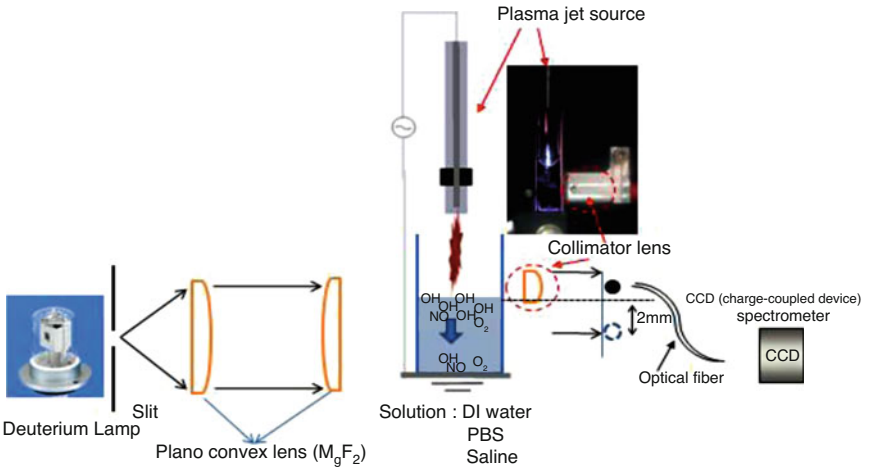

Fig. 3.14 Schematic experimental setup of ultraviolet absorption spectroscopy inside the biosolutions [21]

spectroscopy when the nonthermal plasma has been bombarded onto the biosolution surface. Figure 3.14 shows the schematic experimental setup for the ultraviolet absorption spectroscopy inside the biosolutions. This system consists of deuterium UV lamp in this experiment, whose power is 30 W with spectral wavelength between 160 nm and 800 nm, plano-convex lens whose transmission wavelength ranges are from ultraviolet to infrared, double slit connected to the collimator lens, and CCD spectrometer with optical fiber whose spectral range is from 200 to 1100 nm. The light of UV lamp has been incident and focused by 3 mm plano-convex lens in front of detector system for the measurement of absorption profiles occurred at 309 nm, of the hydroxyl radical OH species [21, 22], as shown in the Fig. 3.14. This detector system consists of double slit in this experiment, whose slit width 100 um and their gap is 1 mm, and then collimator lens has been connected to the optical fiber whose diameter is 500 um. With this experimental situation, we observed no stray light from above the surface since the plasma jet has been bombarded onto the central surface region in the measurement [21].

The hydroxyl OH radical density inside the biosolution, which is generated by the argon nonthermal plasma jet interaction with DI water surface, could be obtained by ultraviolet absorption spectroscopy using the Lambert–Beer's law [22]. The incident UV light incident on the biosolution has the intensity I_o and the transmitted light intensity is denoted by I_v after passing through the OH existing region $x = 10$ mm in this experiment, inside the biosolution, in which the hydroxyl OH radical species are generated by the nonthermal plasma bombardment onto the solution surface. The density of hydroxyl radical species, OH, inside the biosolution, which is induced by the nonthermal plasma bombardment onto the biosolution is given by [22]

$$N = -\frac{1}{\sigma \cdot x} \ln\left(\frac{I v}{I_0}\right) \tag{3.12}$$

where N is the density or concentration for absorbing species of hydroxyl OH radicals, σ is the cross-sectional area of about 1.2×10^{-16} cm^2 for absorbing species of hydroxyl radical OH species [22]. The hydroxyl radical OH density inside the biosolution could be obtained Eq. (3.12), by measurement of the ratio I_v/I_o of the transmitted intensity to the incident one during nonthermal plasma irradiation onto the biosolution. Here the optimized gas flow condition has been also investigated for maximizing the density of hydroxyl OH radical species inside the biosolution under the argon nonthermal plasma jet bombardment onto the solution. The hydroxyl radical density has been investigated at the region of 2 mm above the interfacial solution surface [23], where the UV passing length is 3 mm, as well as inside the biosolution whose spatial passing length is 10 mm, by the ultraviolet absorption spectroscopy by using the deuterium lamp in Ar gas flow ranged from 100 sccm to 350 sccm in argon bioplasma jet. To get an absorption spectrum caused by the hydroxyl radical species, two plano-convex lenses have been used for providing parallel UV lights produced from the deuterium lamp and then making a crossing beam with focused diameter of 200 um when transmission through a middle position of the biosolution along the passing way of 10 mm. The deuterium lamp is a gas-discharged light source, which operates with similar process to arc lamp and has a continuous spectrum from 200 nm to 500 nm in this experiment. After passing through the plasma region of 3 mm located 2 mm above the interfacial surface as well as inside the biosolutions whose passing length is 10 mm, the parallel UV lights whose beam diameter is around 0.5 mm are provided by the convex lenses for UV collection to the optical fiber with collimator lens. At this time the position of the optical lens system has been fixed during the measurement. Here, the spatial resolution of the system is enough for about 1 mm resolution since the output UV has beam diameter of around 0.5 mm. For the measurement of OH radical species at the different position inside the biosolution, only the detector of optical fiber could be moved from the region of 2 mm below water surface by spatial resolution 1 mm without moving of optical lens and collimation system.

Figure 3.15 shows the absorption profile around 309 nm of hydroxyl OH radical species (a) and density of hydroxyl OH radical species (b) at the region of 2 mm above the DI water, respectively, versus the Ar gas flow rates ranged from 100 sccm to the 350 sccm, under the low electrical power of 4.9 W and driving frequency of 35 kHz. It is noted that these measurement values are within 5% error ranges. For the gas flow rate of around 250 sccm, it is found that the density of hydroxyl OH radical species reaches the maximum value of 5.2×10^{15} cm^{-3}. It is also noted that this density of OH radical species has been rapidly decreased to 3.1×10^{15} cm^{-3} as the gas flow rate is increased to 350 sccm in this experiment. These OH densities are in relatively good agreement with other results of $(0.3 \sim 7.5) \times 10^{15}$ cm^{-3} reported by other groups under the low contents of water molecules less than 3% in their employed gases of He, N_2, and N_2/O_2 mixtures [27, 28]. They have used a microwave frequency of 2.45 GHz and RF frequency of 13.56 MHz [27, 28] with

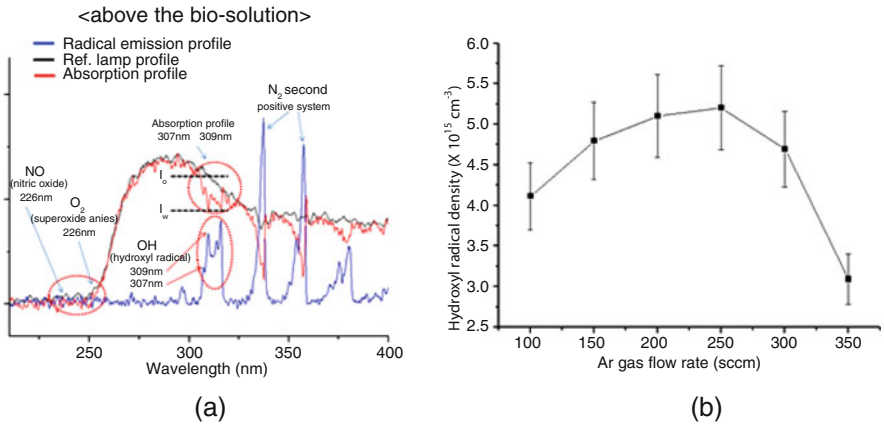

Fig. 3.15 Absorption profile around 309 nm of hydroxyl OH radical species (**a**) and density of hydroxyl OH radical species (**b**) at the region of 2 mm above the DI water, respectively, versus the Ar gas flow rates ranged from 100 sccm to the 350 sccm [21]

relatively high power greater than 100 W. However, we have used the low driving frequency of 35 kHz and low electrical power of 4.9 W in this experiment for the production of OH radical species inside the DI biosolutions by bombardment of the atmospheric pressure nonthermal plasma onto the DI with Ar gas for various ranges of gas flow rates.

3.3 Other ROS Species in Water

Figure 3.16 shows a plot of the OH• (a) and H_2O_2 (b) densities, respectively, denoted by μMole by μMole, nitric acid compounds (c), and especially the NO_3^- ion concentration (d) denoted by mMole, in deionized water activated by the N_2 plasma jet, versus O_2 mole fraction $\xi = n_{O2}/n_0$, where n_{O2} is O_2 density and n_0 is ambient neutral density in the atmospheric pressure at room temperature [29, 30]. The N_2 density n_{N2} is then $(1 - \xi)\, n_0$. Most of the hydroxyl molecules are generated at water surface, and some of them can penetrate into water. The theoretical result obtained is least-squared-fitted to the experimental data. Typical error bar is shown in the data, where the size of the error bar is about 8% of its measurement value. We can see that the hydroxyl density is strong at a small ξ, but it quickly disappears as ξ increases to 0.2, corresponding to the O_2 mole fraction of air. Dots in the figure are the experimental data from the averaged value of three times of measurements. The hydroxyl molecules are mostly generated at water surface, and some of them can penetrate into water. At a small mole fraction of oxygen, the hydroxyl density is strong; but as the oxygen mole fraction increases to 0.2, corresponding to the oxygen mole fraction of air, it quickly disappears. At a small value of oxygen mole

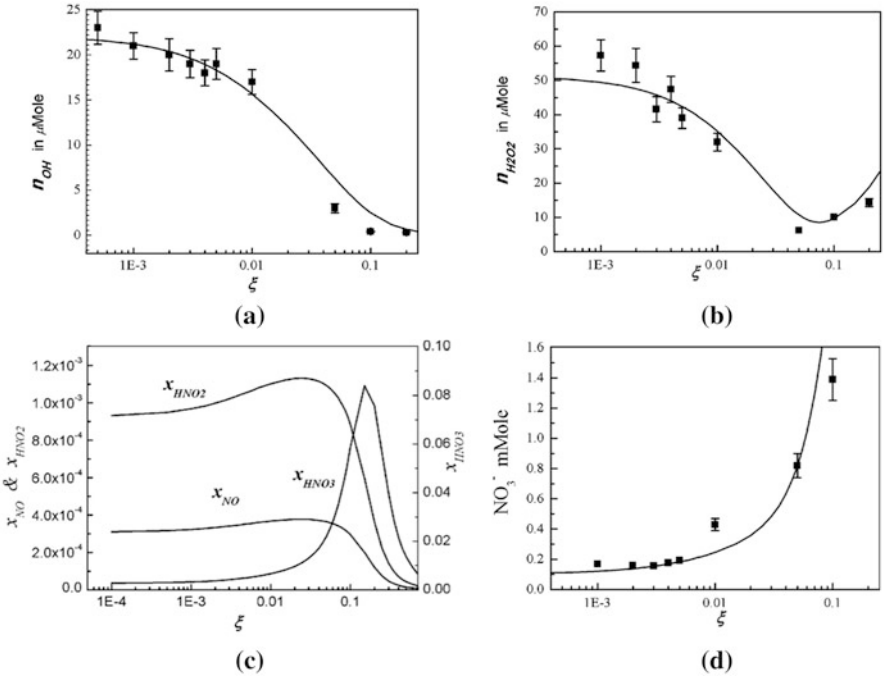

Fig. 3.16 Densities of OH• (**a**), H_2O_2 (**b**) denoted by μMole, nitric acid compounds (**c**), and especially the NO_3^- ion concentration (**d**) denoted by mMole, in deionized water activated by the N_2 plasma jet, versus O_2 mole fraction $\xi = n_{O2}/n_0$, where n_{O2} is O_2 density and n_0 is ambient neutral density in the atmospheric pressure at room temperature [29]

fraction, the intensity of the hydrogen peroxide is very high, where a relatively high intensity of hydroxyl generates H_2O_2, as expected from Fig. 3.16b. But as the oxygen mole fraction increases, its intensity decreases, like the hydroxyl density. However, as the oxygen mole fraction increases to a large value, the hydrogen peroxide density increases again, due to the strong surge of hydrogen dioxide HO_2 molecules. Therefore, as the oxygen mole fraction increases from a small value to a large value, the hydrogen peroxide density decreases, reaches its minimum value at $\xi = 0.05$, and then increases again. The nitric acid compounds are also shown in Fig. 3.16c and d in terms of the O_2 mole fraction. The nitric acid density ($xHNO_3 = nHNO_3/n_0$) is low at a small mole fraction of oxygen, but its intensity increases to a peak value of around $\xi \approx 0.2$, and then decreases, as the ξ increases. Meanwhile, the densities of HNO_2 and NO are at moderate levels in the range of $\xi \leq 0.25$. Note that HNO_3 is a strong acid; meanwhile, HNO_2 is a weak acid. We remind the reader that a moderate level of nitrogen monoxide (NO) exists in the entire range of the O_2 mole fraction. The experimental data of the NO_3^- ion concentration in water is also represented in Fig. 3.16d, in terms of the O_2 mole fraction of ξ. It is shown that nitric acid increases as ξ increases to 0.2; however,

the nitric acid (HNO3) decreases drastically as the ξ increases beyond 0.2 as seen in Fig. 3.16c. The pH value of the plasma activated water, which is slightly alkali without oxygen, decreases to three as ξ increases to 0.25, which can be expected by the nitric acid in Fig. 3.16c, and was also confirmed by experiments. The ξ of ambient air is about 0.2, so that the pH value of water activated by the air plasma is acidic, with $pH \approx 3$.

Solvation of acid species such as HNO_2 and HNO_3 results in the lowering of the water pH. The strong bactericidal activity of water is often attributed to the synergistic action of plasma-generated species in the aqueous phase coupled with low pH [31, 32]. In addition, the effect of alkane-like hydrocarbons, to mimic the chemistry of a biological target, was also investigated in the two-dimensional model study [33]. It was discovered that RNS are unaffected by alkane-like hydrocarbons, whereas ROS were consumed leaving alkyl radicals to reach the tissue target. The major mode in RONS delivery is through convection and diffusion of neutral species into the liquid resulting in overall lower RONS concentrations after plasma treatment. However, the RONS delivery could be synergistically done through plasma initiated UV photolysis [34] and diffusion processes during plasma exposure on liquid or tissues. Another important consideration for applications of air DBD plasmas jet in plasma medicine is that the plasma is usually operated at a frequency in the few tens of kHz—few MHz ranges and the treatment time can be in the order of seconds to minutes. It was found that the spatial location of the plasma plume strongly affects the spatial distribution of the solvated species such as OH and H_2O_2, which have high rates of solvation. Species with low rates of solvation, such as NO, are weakly affected by the location of the plasma plume because of their diffusion in air resulting in a uniform distribution directly above the liquid surface [35].

Acknowledgements This work was supported by the National Research Foundation of Korea (NRF) grant supported by Korea Government (MSIP) (NRF-2016K1A4A3914113 and NRF-2010-0027963) and in part by Kwangwoon University, Seoul, Korea.

References

1. J.-H. Lee, E.-H. Choi, K.-M. Kim, K.-N. Kim, Corrigendum: Effect of non-thermal air atmospheric pressure plasma jet treatment on gingival wound healing. J. Phys. D: Appl. Phys. **49**, 249501 (2016)
2. P. Shaw, N. Kumar, H.S. Kwak, J.H. Park, H.S. Uhm, A. Bogaerts, E.H. Choi, P. Attri, Bacterial inactivation by plasma treated water enhanced by reactive nitrogen species. Sci. Rep. **8**, 11268 (2018)
3. J.-S. Kwon, Y.H. Kim, E.H. Choi, K.-N. Kim, The effects of non-thermal atmospheric pressure plasma jet on attachment of osteoblast. Curr. Appl. Phys. **13**, S42–S47 (2013)
4. K.Y. Baik, Y.H. Kim, Y.H. Ryu, H.S. Kwon, G. Park, H.S. Uhm, E.H. Choi, Feeding-gas effects of plasma jets on Escherichia coli in physiological solutions. Plasma Process. Polym. **10**, 235–242 (2013)
5. N.K. Kaushik, N. Kaushik, N.N. Linh, B. Ghimire, A. Pengkit, J. Sornsakdanuphap, S. Lee, E.H. Choi, Plasma and nanomaterials: fabrication and biomedical applications. Nano **9**, 98 (2019)

6. S.H. Ki, K.Y. Baik, E.H. Choi, Effects of humidity on room disinfection by dielectric barrier discharge plasma. J. Phys. D., accepted for publication **52**, 425204 (2019)
7. M.S. Mann, R. Tiede, K. Gavenis, G. Daeschein, R. Bussiahn, K.-D. Weltmann, S. Emmert, T. von Woedtke, R. Ahmed, Introduction to DIN-specification 91315 based on the characterization of the plasma jet kINPen® MED. Clin. Plasma Med. **4**, 35–45 (2016)
8. J.H. Ahn, Study on optical diagnostics of radical density in non-thermal atmospheric pressure plasma, MS thesis, Kwangwoon University, Korea, 2017
9. N. Kang, S. Oh, Determination of the absolute nitrogen atom density in an Ar-N2 ICP discharge. J. Phys. Soc. **59**(5), 3031–3036 (2011)
10. M. Capitelli, C.M. Ferreora, B.F. Gordiets, A.I. Osipov, *Plasma Kinetics in Atmospheric Gases* (Springer Science & Business Media, Berlin, 2013), p. 196
11. D. Mariotti, Y. Shimizu, T. Sasaki, N. Koshizaki, Method to determine argon metastable number density and plasma electron temperature from spectral emission originating from four 4p argon levels. Appl. Phys. Lett. **89**, 201502 (2006)
12. J. Sornsakdanuphap, P. Suanpoot, Y.J. Hong, B. Ghimire, G. Cho, H.S. Uhm, D. Kim, Y.J. Kim, E.H. Choi, Electron temperature and density of non-thermal atmospheric pressure argon plasma jet by convective wave packet model. J. Korean Phys. Soc. **70**(11), 979–989 (2017)
13. E. Karakas, M.A. Akman, M. Laroussi, The evolution of atmospheric-pressure low-temperature plasma jets: Jet current measurements. Plasma Sources Sci. Technol. **21**, 034016 (2012)
14. E.J. Baek, H.M. Joh, S.J. Kim, T.H. Chung, Effects of the electrical parameters and gas flow rate on the generation of reactive species in liquids exposed to atmospheric pressure plasma jets. Phys. Plasmas **23**, 073515 (2016)
15. Z. Xiong, X. Lu, Q. Xiong, Y. xian, C. Zou, J. Hu, W. Gong, J. Liu, Z. Jiang, Y. Pan, IEEE Trans. Plasma Sci. **38**, 1001 (2010)
16. E. Karakas, M. Laroussi, Experimental studies on the plasma bullet propagation and its inhibition. J. Appl. Phys. **108**, 063305 (2010)
17. S.B. Bayram, P.T. Arndt, Rotational spectra of N2+: an advanced undergraduate laboratory in atomic and molecular spectroscopy. Am. J. Phys. **83**, 867 (2015)
18. N.U. Rehman, M.A. Khan, M.Y. Naz, M. Shafiq, M. Zakaullah, Characterization of 13.56 MHz RF Ne–N2 mixture plasma using intrusive and non-intrusive diagnostic techniques. Phys. Scr. **88**, 045503 (2013)
19. P. Bruggeman, G. Cunge, N. Sadeghi, Plasma Sources Sci. Technol. **21**, 035019 (2012)
20. B. Ghimire, J. Sornsakdanuphap, Y.J. Hong, H.S. Uhm, K.-D. Weltmann, E.H. Choi, The effect of the gap distance between an atmospheric-pressure plasma jet nozzle and liquid surface on OH and N2 species concentrations. Phys. Plasmas **24**, 073502 (2017). https://doi.org/10.1063/1.4989735
21. Y.H. Kim, Y.J. Hong, K.Y. Baik, G.C. Kwon, J.J. Choi, G.S. Cho, S. Uhm, D.Y. Kim, E.H. Choi, Measurement of reactive hydroxyl radical species inside the biosolutions during non-thermal atmospheric pressure plasma jet bombardment onto the solution. Plasma Chem. Plasma Process. **34**, 457 (2014)
22. H.P. Dorn, R. Neuroth, A. Hofzumahaus, Investigation of OH absorption cross sections of rotational transitions in the A2S+, v0 = 0 X2Õ, v00 = 0 band under atmospheric conditions: Implications for tropospheric long-path absorption measurements. J. Geophys. Res. **100**, 7397 (1995)
23. Y.J. Hong, C.J. Nam, K.B. Song, G.S. Cho, H.S. Uhm, D.I. Choi, E.H. Choi, Measurement of hydroxyl radical density generated from the atmospheric pressure bioplasma jet. J. Instrum. **7**, C03046 (2012)
24. G.H. Dieke, H.M. Crosswhite, The ultraviolet bands of OH fundamental data. J. Quant. Spectrosc. Radiat. Transf. **2**, 97 (1961)
25. B. Benstaali, P. Boubert, B.G. Cheron, A. Addou, J.L. Brisset, Density and rotational temperature measurements of the OH and NO radicals produced by a gliding arc in humid air. Plasma Chem. Plasma Process. **22**, 553 (2002)

26. B.G. Kwon, J. Yoon, Superoxide anion radical: principle and application. J. Korean Ind. Eng. Chem. **20**, 593 (2009)
27. N. Srivastava, C. Wang, Effects of water addition on OH radical generation and plasma properties in an atmospheric argon microwave plasma jet. J. Appl. Phys. **110**, 053304 (2011)
28. M. Baeva, K. Rackow, M.M. Becker, J. Ehlbeck, D. Loffhagen, Characterization of atmospheric pressure microwave plasma in N2/O2/H2O gas mixtures. Topic C9, 30th ICPIG, Belfast, Northern Ireland UK, 2011
29. H.S. Uhm, S.H. Ki, K.Y. Baik, E.H. Choi, Influence of oxygen on generation of reactive chemicals from nitrogen plasma jet. Sci. Rep. **8**, 9318 (2018)
30. A.S. Blecker, R. Bansemer, S. Reuter, K.D. Weltmann, How to produce an NOx-instead of Ox-based chemistry with a cold atmospheric plasma jet. Plasma Process. Polym. **13**, 1120 (2016)
31. M. Naïtali, G. Kamgang-Youbi, J. Herry, M. Bellon-Fontaine, J. Brisset, Combined effects of long-living chemical species during microbial inactivation using atmospheric plasma-treated water. Appl. Environ. Microbiol. **76**, 7662–7664 (2010)
32. J. Julák, V. Scholtz, S. Kotúčová, O. Janoušková, The persistent microbicidal effect in water exposed to the corona discharge. Phys. Med. **28**, 230–239 (2012)
33. W. Tian, M. Kushner, Atmospheric pressure dielectric barrier discharges interacting with liquid covered tissue. J. Phys. D. Appl. Phys. **47**, 165201 (2014)
34. P. Attri, Y. Kim, D. Park, J. Park, Y. Hong, H. Uhm, K. Kim, A. Fridman, E.H. Choi, Generation mechanism of hydroxyl radical species and its lifetime prediction during the plasma-initiated ultraviolet (UV) photolysis. Sci. Rep. **5**, 9332 (2015)
35. A. Starikovskiy, Y. Yang, Y. Cho, A. Fridman, Non-equilibrium plasma in liquid water: Dynamics of generation and quenching. Plasma Sources Sci. Technol. **20**, 024003 (2011)